

The evolution towards the rod-like axisymmetric structure for turbulent stress tensor

Yi Li

Citation: [Physics of Fluids](#) **27**, 085104 (2015); doi: 10.1063/1.4928245

View online: <http://dx.doi.org/10.1063/1.4928245>

View Table of Contents: <http://scitation.aip.org/content/aip/journal/pof2/27/8?ver=pdfcov>

Published by the [AIP Publishing](#)

Articles you may be interested in

[On the evolution of the invariants of the velocity gradient tensor in single-square-grid-generated turbulence](#)

Phys. Fluids **27**, 075107 (2015); 10.1063/1.4926472

[Influence of vortex dynamics and structure on turbulence statistics at large scales](#)

Phys. Fluids **27**, 055106 (2015); 10.1063/1.4921210

[Drag reduction effect by a wave-like wall-normal body force in a turbulent channel flow](#)

Phys. Fluids **26**, 115104 (2014); 10.1063/1.4901186

[Tetrahedron deformation and alignment of perceived vorticity and strain in a turbulent flow](#)

Phys. Fluids **25**, 035101 (2013); 10.1063/1.4795547

[Structure information in rapid distortion analysis and one-point modeling of axisymmetric magnetohydrodynamic turbulence](#)

Phys. Fluids **12**, 2609 (2000); 10.1063/1.1287838

The logo for Oxford Language Editing. It features the words 'OXFORD LANGUAGE EDITING' in a bold, blue, sans-serif font. To the right of the text is a stylized graphic of a paper airplane or a pen nib, colored in shades of blue and red, pointing upwards and to the right.

English language support
for academic researchers
worldwide

OXFORD
UNIVERSITY PRESS

The evolution towards the rod-like axisymmetric structure for turbulent stress tensor

 Yi Li^{a)}
School of Mathematics and Statistics, University of Sheffield, Sheffield S3 7RH, United Kingdom

(Received 20 May 2015; accepted 28 July 2015; published online 11 August 2015)

Modelling the turbulent stress tensor is a main task for both large eddy simulations and methods based on Reynolds averaged Navier-Stokes equations. The turbulent stress is known as the subgrid-scale stress in the former and the Reynolds stress in the latter. In this paper, we examine the observation that the stress tensor tends to evolve towards a rod-like axisymmetric configuration. This observation has been well documented for the subgrid-scale stress. However, for the Reynolds stress, the available data are still too limited to draw a definite conclusion. In the first part of the paper, we show that the tendency is also universal for the Reynolds stress by direct numerical simulations of decaying anisotropic turbulence. To show the universality, it is crucial to examine the decaying process from initial turbulent fields with a wide range of levels of anisotropy. Such initial fields are generated by a novel synthetic turbulence model based on the so-called constrained multi-turnover Lagrangian map. In the second part, we use the direct numerical simulation data to study the dynamical mechanisms of the evolution towards the rod-like structures. Among others, the analyses show that the nonlinear self-interaction term is the driving force of the process, and that the pressure tends to enhance the disk-like axisymmetric structure but overall tends to reduce the anisotropy of the stress tensor. The results shed light on the subtle difference between the pressure and the nonlinear self-interaction terms. © 2015 AIP Publishing LLC. [<http://dx.doi.org/10.1063/1.4928245>]

I. INTRODUCTION

We investigate in this paper a common feature observed in the turbulent stress tensors for both large eddy simulations (LESs) and the methods based on the Reynolds averaged Navier-Stokes (RANS) equations. In LES, the filtered Navier-Stokes (NS) equations are the governing equations, which read

$$\partial_t \tilde{u}_i + \tilde{u}_j \partial_j \tilde{u}_i = -\partial_i \tilde{p} - \partial_j \tau_{ij} + \nu \nabla^2 \tilde{u}_i. \quad (1)$$

In the above equations, \tilde{u}_i is the filtered velocity,

$$\tilde{u}_i(\mathbf{x}) = \int G_\Delta(\mathbf{x} - \mathbf{y}) u_i(\mathbf{y}) d\mathbf{y}, \quad (2)$$

where G_Δ is the filter with length scale Δ . \tilde{p} is the filtered pressure defined in a similar way and $\tau_{ij} \equiv \tilde{u}_i \tilde{u}_j - \tilde{u}_i \tilde{u}_j$ is the subgrid-scale (SGS) stress. Density $\rho = 1$ has been assumed. ν is the kinematic viscosity. The equations are not closed, because the SGS stress τ_{ij} has to be modelled.¹⁻³

In RANS, one considers the ensemble averaged NS equations.³ In this case, one has to model the Reynolds stress $R_{ij} \equiv \langle u_i u_j \rangle$, where $\langle \cdot \rangle$ denotes ensemble average. We have assumed $\langle u_i \rangle = 0$, which is sufficient for the discussion in this paper because we consider only homogeneous turbulence in which the mean velocity gradient is zero. We note that ensemble average is the same as

^{a)}Email: yili@sheffield.ac.uk.

spatial average for such flows. Therefore, the Reynolds stress has no fundamental difference from the SGS stress when a non-negative filter is used for the latter.

To close the Reynolds stress tensor R_{ij} , one may include its transport equation as part of the governing equations and model the unclosed terms. In homogeneous turbulence with no mean velocity ($\langle u_i \rangle = 0$), the equation for R_{ij} becomes

$$\frac{dR_{ij}}{dt} = \langle p(\partial_j u_i + \partial_i u_j) \rangle - 2\nu \langle \partial_k u_i \partial_k u_j \rangle. \quad (3)$$

The two terms on the right hand side are the slow pressure-strain-rate correlation and the viscous dissipation, respectively. Various models have been proposed for the two terms (see, e.g., Ref. 3, and the reference therein). Direct numerical simulations (DNS) and experiments in decaying homogeneous anisotropic turbulence have found that the initially anisotropic R_{ij} relaxes back to isotropy during the decaying process. The models are required to reproduce the correct behaviours for R_{ij} during this so-called return-to-isotropy process (RIP).

To describe the anisotropy of the Reynolds stress tensor, one may use the anisotropic tensor

$$b_{ij} = \frac{R_{ij}}{R_{kk}} - \frac{1}{3} \delta_{ij}. \quad (4)$$

b_{ij} may be characterized by its tensor invariants, which can be defined as

$$I_{2b} = \frac{1}{2} b_{ij} b_{ji}, \quad I_{3b} = \frac{1}{3} b_{ij} b_{jk} b_{ki}, \quad (5)$$

or

$$\eta = (I_{2b}/3)^{1/2}, \quad \xi = (I_{3b}/2)^{1/3}. \quad (6)$$

Realizability of R_{ij} implies that the possible values for ξ and η are limited in the so-called Lumley triangle,³⁻⁶ as is illustrated in Fig. 1 (Note that using variables (I_{3b}, I_{2b}) , one also obtain a triangular area although the boundaries are not straight lines³). The right boundary $\eta = \xi$ corresponds to axisymmetric configurations in which b_{ij} has one large positive eigenvalue and two equal negative eigenvalues, whereas on the left boundary b_{ij} has two equal positive eigenvalues and a negative eigenvalue with larger magnitude. The former configuration has been termed “rod-like,” while the latter “disk-like,”⁶ referring to the shapes of the tensor ellipsoids corresponding to the two conditions, respectively.

During the RIP, the state of the Reynolds stress tensor changes over time. The changes are represented by a trajectory on the (ξ, η) plane. Different initial conditions correspond to different trajectories. Previous DNS and experimental data are summarized in, e.g., Refs. 3, 7, and 8. The data show that the trajectories are curves rather than straight lines. The observation implies that the pressure-strain-rate term is nonlinear in b_{ij} . As a consequence, different nonlinear models have been proposed to replace the classical linear Rotta model, as is shown in, e.g., Refs. 7–11. A detailed summary and appraisal can be found in Refs. 3, 7, and 12. On the other hand, although the data

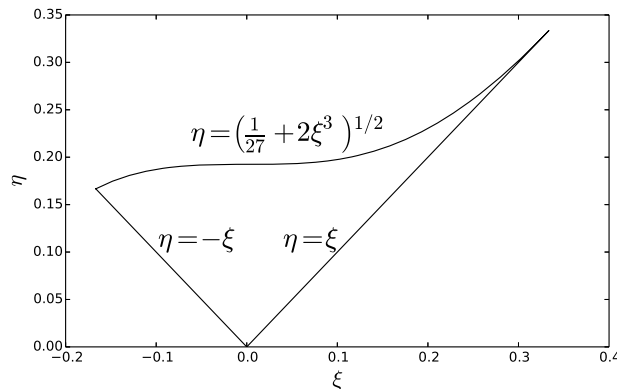


FIG. 1. Sketch of the Lumley triangle in the (ξ, η) plane.

are sufficient to show the deviation from the linear relaxation, they are not conclusive regarding the details of the trajectories. In particular, the data seem to suggest that the trajectories tend to evolve towards the right boundary of the Lumley triangle (corresponding to the rod-like axisymmetric state), before they relax towards the origin (corresponding to the isotropic state). However, the universality of this trend is still in question because the available data cover only a small range of initial states close to the rod-like state. It is not clear if the same tendency still exists if the initial state is far from the rod-like state. As a matter of fact, some nonlinear models (e.g., Refs. 7 and 11) predict that the trajectories would cross over from the left half of the phase plane (where $\xi < 0$) to the right ($\xi > 0$) and approach the right boundary, whereas some other models predict a tendency towards the left boundary of the Lumley triangle (corresponding to the disk-like axisymmetric structure) when the initial state is on the left half of the phase plane.⁸ Currently, there are no data available to either confirm or reject these predictions. One of the goals of this article is to provide data to fill this gap.

To do so, we will need to simulate the RIP starting from initial conditions that have not been looked into before. The technical challenge is to generate realistic initial turbulence field with controlled anisotropic tensor b_{ij} that is also divergence-free and homogeneous. Existing DNS has used precursor simulations, in which mean strain is applied to a homogeneous turbulent field to generate anisotropy.^{13,14} As mentioned above, the anisotropic states having been obtained mostly cluster around the boundaries of the Lumley triangle. To achieve our goal, we make use of the constrained multi-scale turn-over Lagrangian map (CMTLM) proposed recently in Ref. 15. In the multi-scale turn-over Lagrangian map (MTLM)^{16,17} method, a synthetic field is generated by advecting fluid particles in a random Gaussian field recursively over a set of increasingly refined meshes. The process gives rise to a highly non-Gaussian velocity field that reproduces very well a whole range of statistics of real incompressible isotropic turbulence.¹⁵⁻¹⁸ CMTLM formulates MTLM as an optimization problem with the Gaussian random input as the control and some given velocity field as the target. As such, CMTLM can generate inhomogeneous synthetic incompressible turbulence while retaining the realistic small scale statistics in MTLM. Thus, CMTLM provides a viable tool for current study. Therefore, as part of the first goal of this paper, we generalize the CMTLM method to produce synthetic incompressible turbulence with prescribed anisotropic Reynolds stress. We then use the synthetic fields as initial conditions for the simulations of the return-to-isotropy process.

As we will show below, the data show that the tendency towards the rod-like configuration is indeed to large extent universal. This tendency is reminiscent of the same observation for the SGS stress tensor. Let $\tau_{ij}^d \equiv \tau_{ij} - \tau_{kk}\delta_{ij}/3$ be the deviatoric part of the SGS tensor. The invariants of τ_{ij}^d are denoted as

$$I_{2\tau} = \frac{1}{2}\tau_{ij}^d\tau_{ji}^d, \quad I_{3\tau} = \frac{1}{3}\tau_{ij}^d\tau_{jk}^d\tau_{ki}^d. \quad (7)$$

Because the SGS stress is a random variable, it has a range of possible geometrical configurations. Nevertheless, the joint probability density function (PDF) of $I_{2\tau}$ and $I_{3\tau}$ shows strong peak values around the right boundary of the Lumley triangle, indicating that it is much more probable to observe the rod-like axisymmetric state (see, e.g., Ref. 19 and below) for the SGS stress tensor too.

Given the universality of the observation, it is of interests to understand its dynamical mechanisms, and this is the second goal of this paper. To do so, we look into the dynamical equations for the tensor invariants. To simplify the calculation, we first approximate the SGS stress tensor with the nonlinear model.²⁰⁻²² We then use DNS data to evaluate the contributions from nonlinear self-interaction, pressure, SGS interactions, and viscous diffusions, separately. We use the transport equation for the joint PDF for the invariants and the conditional statistics^{23,24} in the phase space to illustrate the different behaviours of each contribution hence show that the driving mechanism towards the structure is the nonlinear self-interaction term.

The paper is organized as follows. In Section II, we explain briefly the CMTLM method and discuss some properties of the synthetic fields. In Section III, we present the DNS data and the observation about the evolution towards the rod-like axisymmetric configuration. The physical mechanism of the process is discussed in Section IV. Conclusions are drawn in Section V. In the

appendices, we document the details of the CMTLM method as well as some of the coefficients in the dynamical equations for the tensor invariants.

II. THE CMTLM SYNTHETIC VELOCITY FIELDS WITH PRESCRIBED REYNOLDS STRESS

We explain in this section how to generate the initial velocity fields with prescribed Reynolds stress tensor using the CMTLM method.¹⁵ CMTLM is an extension of the MTLM,¹⁷ which maps a Gaussian random velocity field to a realistic non-Gaussian synthetic turbulent field. The detail of the map is given in [Appendix A](#). Here, it suffices to denote the map by \mathcal{M} and write

$$\mathbf{u} = \mathcal{M}\boldsymbol{\varphi}, \quad (8)$$

where \mathbf{u} is the synthetic velocity field, and $\boldsymbol{\varphi}$ is the Gaussian random input. Both are three dimensional vector fields with given energy spectrum $E_p(k)$. The synthetic field \mathbf{u} has been extensively studied previously.¹⁵⁻¹⁸

Apparently, one obtains different \mathbf{u} for different $\boldsymbol{\varphi}$. In CMTLM, we choose suitable $\boldsymbol{\varphi}$ to obtain a synthetic \mathbf{u} that has additional features, including inhomogeneous mean flows etc.¹⁵ Such a $\boldsymbol{\varphi}$ is found by solving a constrained optimization problem. In a generic case, the cost function measures the difference between the MTLM synthetic field and a given target velocity field $\mathbf{w}(\mathbf{x})$ and is defined as

$$J_{\text{generic}}(\mathbf{u}) = \frac{1}{2} \|\mathcal{F}(\mathbf{u} - \mathbf{w})\|_2^2. \quad (9)$$

\mathcal{F} is a filter which extracts the features in $\mathbf{u}(\mathbf{x})$ and $\mathbf{w}(\mathbf{x})$ that we would like to match. \mathbf{u} is given by Eq. (8). We take $\boldsymbol{\varphi}$ as the control of the optimization problem and aim at finding an optimal $\boldsymbol{\varphi}$ that minimizes J_{generic} subject to the constraint Eq. (8).

To study the return-to-isotropy process, we need to produce a set of homogeneous turbulent velocity fields with prescribed anisotropic Reynolds stress tensor. Let R_{ij}^0 be the prescribed Reynolds stress tensor. Instead of using R_{ij}^0 as the target in the cost function, we use the corresponding anisotropic tensor b_{ij}^0 , which is defined by R_{ij}^0 in the same way as in Eq. (4). Specifically, we define the cost function for the synthetic field \mathbf{u} as follows:

$$J(\mathbf{u}) = \frac{1}{2} (2\pi)^3 [\bar{b}_{ij} - b_{ij}^0]^2 \langle \bar{u}_k \bar{u}_k \rangle^2, \quad (10)$$

where \bar{u}_k is the filtered synthetic velocity field and \bar{b}_{ij} is the corresponding anisotropic tensor, i.e.,

$$\bar{b}_{ij} = \frac{\langle \bar{u}_i \bar{u}_j \rangle}{\langle \bar{u}_k \bar{u}_k \rangle} - \frac{1}{3} \delta_{ij}. \quad (11)$$

\bar{u}_k is defined by $\bar{u}_k = G_c * u_k$, where u_k is the k th component of $\mathbf{u} (\equiv \mathcal{M}\boldsymbol{\varphi})$ and G_c is the cutoff filter with filter scale L_c . \bar{b}_{ij} is a functional of the synthetic field \mathbf{u} . When J is small, the anisotropic tensor b_{ij} of the synthetic field \mathbf{u} would be close to the prescribed b_{ij}^0 .

We have chosen to use b_{ij}^0 as the target because it is easier to enforce realizability conditions. The factor $(2\pi)^3$ in Eq. (10) is the volume of the periodic domain. We have also decided to match \bar{b}_{ij} , instead of b_{ij} , with b_{ij}^0 . Because the contributions to the Reynolds stress come mainly from the very large scales, \bar{b}_{ij} is not much different from b_{ij} . Therefore, optimizing \bar{b}_{ij} is practically the same as optimizing b_{ij} . On the other hand, as will be seen below, the adjoint variable will be non-zero only for wave number less than π/L_c due to the filtering. Thus, the filtering has the advantage of reducing the computational cost. Throughout this study, we use $L_c = \pi/6$.

To find the optimal $\boldsymbol{\varphi}$ that minimizes J , we use the adjoint-based method (see, e.g., Refs. 15 and 25). We introduce the adjoint variable $\boldsymbol{\xi}(\mathbf{x})$ and define the Lagrangian,

$$\mathcal{L}(\mathbf{u}, \boldsymbol{\xi}, \boldsymbol{\varphi}) = J(\mathbf{u}) + \int \boldsymbol{\xi} \cdot (\mathbf{u} - \mathcal{M}\boldsymbol{\varphi}) d\mathbf{x}. \quad (12)$$

We thus find the adjoint equation,

$$\begin{aligned} \xi_i(\mathbf{x}) = & -2\langle \bar{u}_k \bar{u}_k \rangle [\bar{b}_{ij} - b_{ij}^0] \bar{u}_j(\mathbf{x}) \\ & + 2\langle \bar{u}_k \bar{u}_k \rangle [\bar{b}_{mn} - b_{mn}^0] b_{mn}^0 \bar{u}_i(\mathbf{x}). \end{aligned} \quad (13)$$

We also find the gradient of the cost function with respect to the control φ ,

$$\frac{\mathcal{D}J}{\mathcal{D}\varphi} = -\mathcal{M}^+ \xi, \quad (14)$$

where \mathcal{M}^+ is the adjoint operator of the tangent operator of \mathcal{M} . \mathcal{M}^+ has the same expression as the one in Ref. 15, which is also given in Appendix A. The functional derivative is understood in the Gateaux sense.²⁵

The optimization problem is solved from Eqs. (8), (13), and (14), using the steepest descent method with back tracking.^{15,25,26} The solution provides the optimal control φ and the corresponding optimal synthetic field \mathbf{u} . Note that in our previous work,¹⁵ we have used the so-called “discretization of the adjoint” formulation, where we derive the continuous versions of the adjoint equation and gradient of the cost function, which are then discretized when they are solved numerically. Here, we have partially used the “adjoint of the discretization” formulation, as we describe in Appendix A.

To illustrate the result of the above CMTLM system, Figs. 2–4 show the contours of the three components of the velocity field on a two dimensional cut of such a CMTLM field (this field is used as the initial condition for one of the samples in Case D below, shown with magenta left-pointing triangles in Fig. 7—see Sec. III for more detail). The velocity field is synthesized on a 128^3 mesh of grids and has an anisotropic tensor with

$$b_{11} = 0.2647, b_{22} = 0.0067, b_{33} = -0.2714 \quad (15)$$

and zero for other components. It is seen from the figures that, among others, the z velocity component tends to have smaller values, consistent with the imposed Reynolds stress tensor.

The energy spectra of the three components are shown in Fig. 5. The low wavenumber parts of the spectra show the expected differences: the z -component is the smallest whereas the x -component is the largest. On the other hand, the difference decreases when wavenumber is increased, and the three spectra almost agree with each other at the high wavenumber end, as one would expect in real turbulence. We note that the CMTLM procedure (and the MTLM procedure) takes a given three dimensional total energy spectrum as input. The componential spectra for the velocity components are not imposed. The anisotropic energy distribution among different components shown in Fig. 5 is generated by the dynamics embedded in the CMTLM procedure.

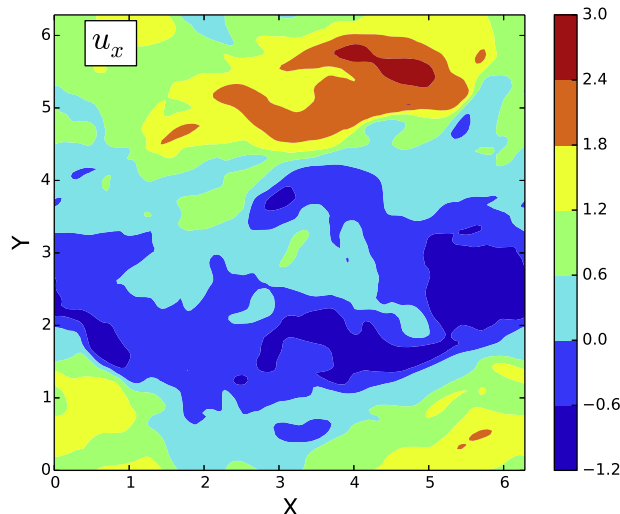
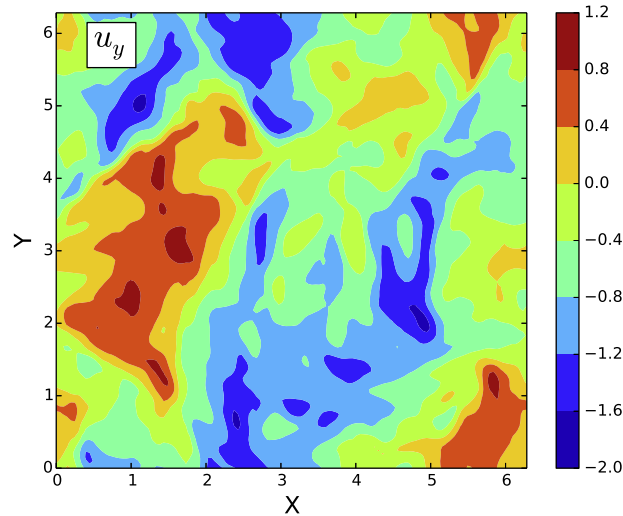


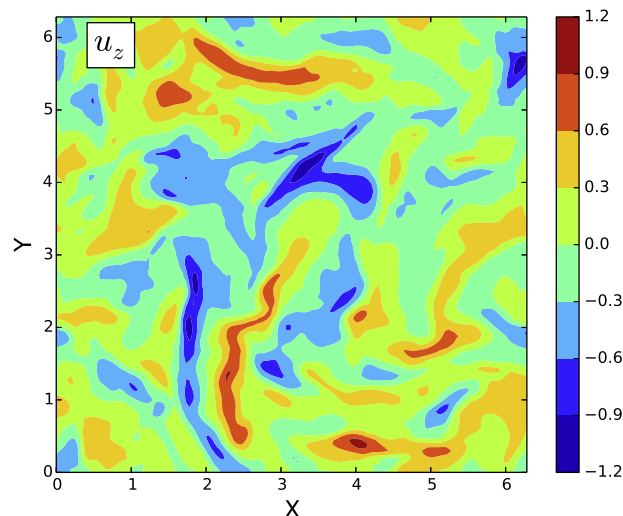
FIG. 2. The contour of the x -component of a CMTLM synthetic velocity field on a two dimensional cut.

FIG. 3. Same as Fig. 2 but for the y -component.

III. EVOLUTION TOWARDS THE ROD-LIKE AXISYMMETRIC STRUCTURE: OBSERVATIONS

In this section, we use the synthetic fields generated by the CMTLM method as the initial fields to perform direct numerical simulations of decaying homogeneous turbulence. We report the results regarding the tendency towards the rod-like axisymmetric configuration for the Reynolds stress tensor and the SGS stress tensor.

Decaying turbulence in a periodic box $[0, 2\pi]^3$ is simulated by the pseudo-spectral method. In total, nine different ensembles of data are generated, each with a different initial Reynolds stress tensor. In each ensemble, about 20 realizations of time series of the three dimensional velocity fields are generated. The statistics are averaged over space and then over all the realizations in each ensemble, then the results from different ensembles are compared. In all nine but one cases, 128^3 grids are used with viscosity $\nu = 0.0032$, whereas 256^3 grids are used in the remaining case with viscosity $\nu = 0.0016$. The viscosity has been chosen to make sure $k_{\max}\ell_K > 1.5$ in both cases, where $\ell_K \equiv [\nu^3/\epsilon(0)]^{1/4}$ is the Kolmogorov length scale based on the initial mean energy dissipation $\epsilon(0)$ and k_{\max} is the maximum resolved wavenumber. We will refer to the first eight cases Case

FIG. 4. Same as Fig. 2 but for the z -component.

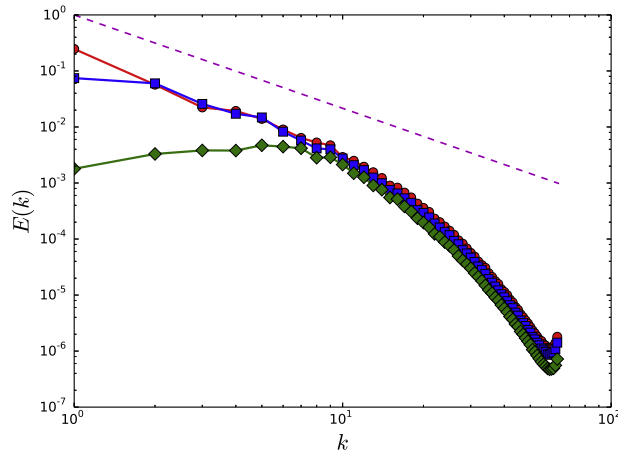


FIG. 5. The energy spectra for the three velocity components of the CMTLM synthetic velocity field shown in Figs. 2–4. Red circles: x -component, blue squares: y -component, and green diamonds: z -component. The dashed line shows the Kolmogorov $-5/3$ spectrum.

A through Case H and the last one (with 256^3 grids), Case I. In all simulations, the two-step Adam-Bashforth method is used to advance in time, with the starting step computed using a second order Runge-Kutta scheme. The Courant number based on the maximum velocity is chosen as 0.15.

Fig. 6 shows the decay of the turbulent kinetic energy $k(t)$ and the mean energy dissipation $\epsilon(t)$, and the skewness factor of the longitudinal velocity gradient \mathcal{S} , where $T_L \approx 6.4$ is the initial large eddy turnover time scale. The figure reproduces the usual observations in decaying turbulence. Notably, because the CMTLM field produces realistic small scale statistics, there is only a very short transition period. The skewness \mathcal{S} reaches its stationary value $\mathcal{S} \approx -0.5$ almost right after the simulations have been started. The dissipation rate peaks at $t = 0$, markedly different from simulations with random Gaussian initial conditions. In the latter cases, the dissipation usually only reaches peak values after about an eddy turnover time in which small scale structures are developed. Therefore, simulations using CMTLM fields as initial conditions capture the decaying process more accurately, especially its early phase.

Next, we calculate the Reynolds stresses and the corresponding anisotropic tensor b_{ij} for all nine ensembles. We also calculate the SGS stress tensor τ_{ij}^d in Case I (with resolution 256^3) and compare its behaviours with those of the Reynolds stress. The Gaussian filter with filter scale Δ is used to calculate the SGS stress tensor.

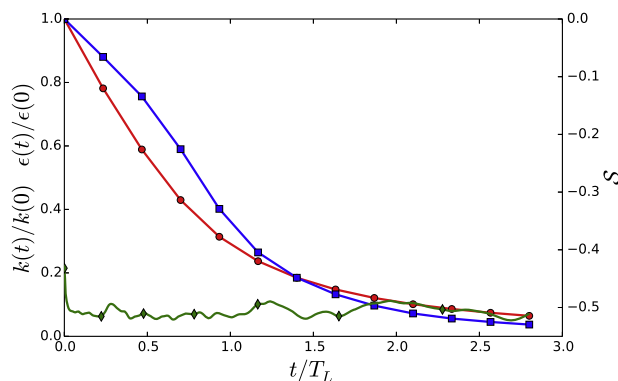


FIG. 6. The decay of the turbulent kinetic energy $k(t)$ and mean energy dissipation $\epsilon(t)$ (left axis), and the skewness factor of the longitudinal velocity gradient \mathcal{S} (right axis) in Case I. Red circles: $k(t)/k(0)$, blue squares: $\epsilon(t)/\epsilon(0)$, and green diamonds: \mathcal{S} .

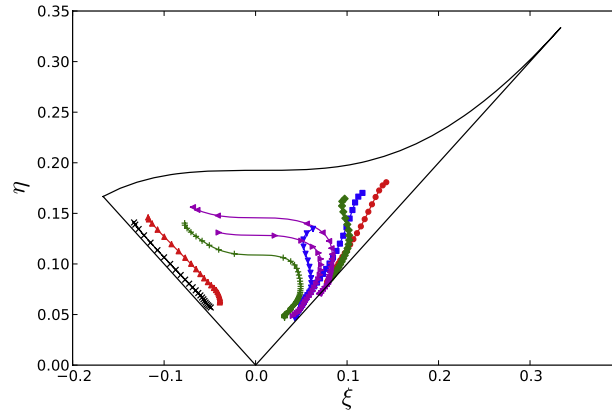


FIG. 7. The relaxation of the anisotropic tensor b_{ij} shown in the Lumley triangle on the (ξ, η) phase plane, from $t/T_L = 0$ to approximately 0.8 for all nine cases. Case A: red circles, Case B: blue squares, Case C: green diamonds, Case D: magenta left-pointing triangles, Case E: black crosses, Case F: red upward-pointing triangles, Case G: blue gradients, Case H: magenta right-pointing triangles, and Case I: green pluses.

We first look at the results for (ξ, η) . The trajectories of the phase point are shown in Fig. 7 for the nine sets of initial conditions. First, we observe that, thanks to the new CMTLM technique, we are able to generate initial fields that cover a wider area in the Lumley triangle. Some of them are far from the left and right boundaries where previous data have been obtained. Second, most of the trajectories show a clear tendency to evolve towards the right boundary, corresponding to the rod-like axisymmetric state. In particular, three trajectories (those shown with left triangles, right triangles, and pluses) originate from the negative half plane, cross over to the right half, and converge to the right boundary. Although no clear trend is observed for the two trajectories originated near the disk-like axisymmetric state (marked by red upward triangles and black crosses), the results nevertheless clearly demonstrate that there is a universal trend towards the rod-like axisymmetric configuration over a majority part of the triangle.

A more quantitative way to characterize the evolution is to use the shape factor²⁷ $s^* \equiv (\xi/\eta)^3$. It can be shown that $-1 \leq s^* \leq 1$ and that $s^* = 1$ for a rod-like axisymmetric state. Thus, we expect that the value of s^* over time will tend to 1, according to the previous figure. Fig. 8 shows s^* as a function of time for the cases shown in Fig. 7. We can see that, in almost all cases, s^* increases towards $s^* = 1$ as time increases. For the two initial conditions close to the disk-like axisymmetric state (shown with red upward triangles and black crosses), Fig. 8 shows that s^* also tends to increase, the amount of change being small notwithstanding. Thus, they also tend to move towards the rod-like axisymmetric state, even though it is not obvious from Fig. 7.

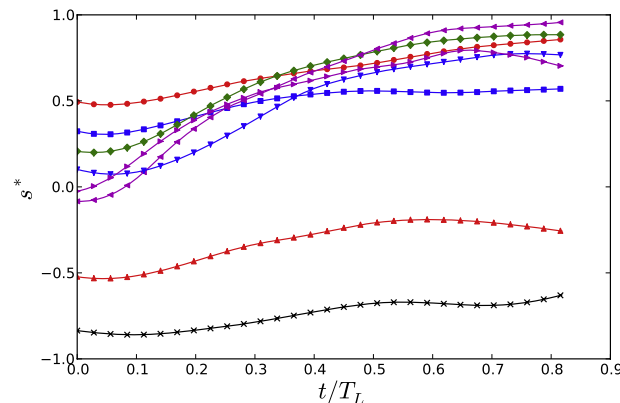


FIG. 8. The evolution of the shape factor s^* for the anisotropic Reynolds stress in all nine cases.

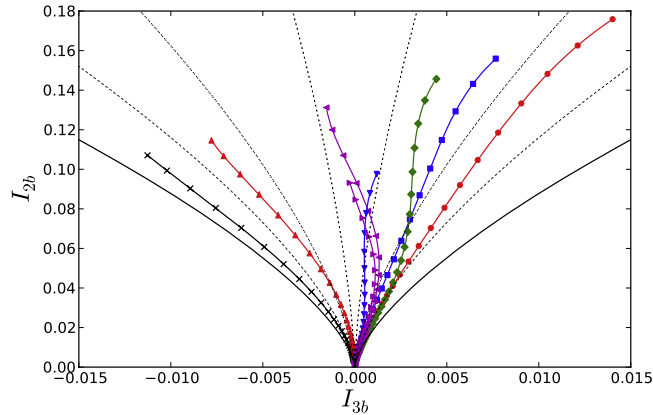


FIG. 9. The evolution of the invariants I_{3b} and I_{2b} for the anisotropic Reynolds stress tensor b_{ij} . The black solid lines represent the left and right boundaries of the Lumley triangle. The black dotted lines corresponds to the trajectories of “linear relaxation” (see text for more detail).

In the literature of SGS modelling, it is more common to use the invariants $I_{2\tau}$ and $I_{3\tau}$ to characterize the SGS stress τ_{ij}^d . Therefore, we also look into the relaxation of the Reynolds stress using I_{2b} and I_{3b} , as is shown in Fig. 9. Because the boundaries of the Lumley triangle are not straight lines in variables I_{3b} and I_{2b} , it is not obvious as to what the trajectories represent. To alleviate this difficulty, we use a linear relaxation process as a reference. If b_{ij} decays linearly, i.e., if

$$\frac{db_{ij}}{dt} = -\alpha b_{ij} \tag{16}$$

for some constant α , then $I_{2b} = CI_{3b}^{2/3}$ for some constant C . We plot with black dotted lines in Fig. 9 this relation for a few values of C . The comparison with these lines now provides clear indication that the trajectories of the phase points bend towards the rod-like axisymmetric configurations, consistent with the results shown in Fig. 7. This linear reference case is also used below when we discuss the dynamics of the process.

The results shown in Figs. 7-9 provide new data for the modelling of the Reynolds stress tensor. We make a few remarks on this aspect briefly, even though it is not our goal to assess or develop models in this paper. First, the results confirm the prediction of some nonlinear pressure-strain-rate correlation models, that the trajectories for (ξ, η) may cross over from the left half plane to the right.^{7,10,11} Second, we do not find indication in our results that there is a tendency towards the disk-like axisymmetric structure as suggested in some models.⁸

We now look into the SGS stress tensor τ_{ij}^d . To compare with the results for the Reynolds stress, we first calculated (ξ, η) for the averaged SGS stress tensor. Fig. 10 shows the trajectories for the Reynolds stress tensor with green pluses and the averaged SGS stress tensor with blue squares. Also plotted is the same statistics for the nonlinear model of the SGS stress (also known as the Clark model, see Sec. IV for more discussion),²¹ defined as

$$T_{ij} = \frac{\Delta^2}{12} \left(\partial_k \tilde{u}_i \partial_k \tilde{u}_j - \frac{1}{3} \delta_{ij} \partial_k \tilde{u}_m \partial_k \tilde{u}_m \right). \tag{17}$$

All trajectories in Fig. 10 display the same trend, namely crossing over to the right half of the phase plane and approaching the rod-like axisymmetric configuration first before relaxing towards the origin. The results for the shape factor, shown in Fig. 11, show consistent behavior. The tendency can also be observed for the joint PDF of the invariants $I_{3\tau}$ and $I_{2\tau}$ of τ_{ij} (cf. Eq. (7)) and the PDF of the corresponding shape factor $s_\tau^* \equiv 3^{3/2} I_{3\tau} / 2 I_{2\tau}^{3/2}$. The latter has been extensively studied in, e.g., Ref. 19. We thus present only a few results for the former to illustrate the behaviors. Fig. 12 shows the joint PDF calculated at several times $t/T_L \approx 0.7, 1.2, 2.1$. The main observation is that high value contours are closely aligned with the right boundary of the Lumley triangle at all times, showing that there is a strong preference for the rod-like axisymmetric state. If we compare the

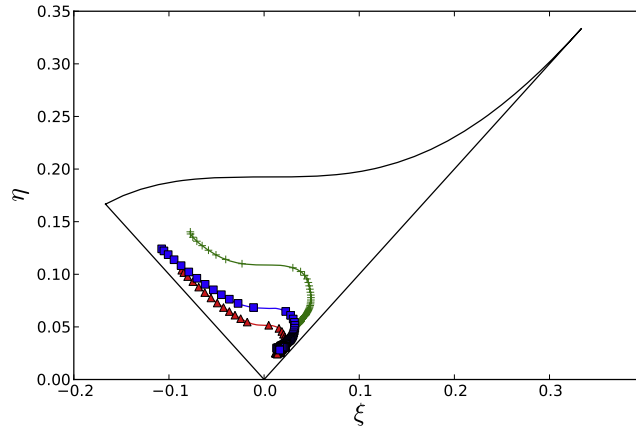


FIG. 10. Relaxation of the mean SGS stress ($\langle\tau_{ij}^d\rangle$, blue squares) and the averaged nonlinear model ($\langle T_{ij}\rangle$, red triangles) in Case I with 256^3 resolution, compared with the results for the anisotropic Reynolds stress (b_{ij} , green pluses). $\Delta = 64\delta x$.

contours at different times, we may see that the contours shrink towards the right boundary as time increases. However, the difference is not large enough to make solid conclusion.

Similar results are observed for the invariants of the nonlinear model T_{ij} , defined as

$$I_{2T} = \frac{1}{2}T_{ij}T_{ji}, \quad I_{3T} = \frac{1}{3}T_{ij}T_{jk}T_{ki}. \tag{18}$$

Fig. 13 shows the joint PDF of I_{2T} and I_{3T} , which displays the same trend as τ_{ij}^d , showing a strong preference for the rod-like axisymmetric configuration.

To summarize, the results presented in this section clearly show that the tendency towards the rod-like axisymmetric configuration is genuine and universal to large extent for both the Reynolds stress, the SGS stress, as well as the nonlinear model. The universal behavior suggests that it is a consequence of some fundamental physical processes in turbulence.

IV. EVOLUTION TOWARDS THE ROD-LIKE AXISYMMETRIC STRUCTURE: DYNAMICS

In this section, we look into the dynamical processes that underline the behavior observed in Sec. III. Given that the Reynolds stress can be considered a limiting case for the SGS stress, we focus on the latter. Our objective is to derive the dynamical equations for the invariants of the SGS stresses and evaluate the contributions of the involved physical processes. However, to simplify

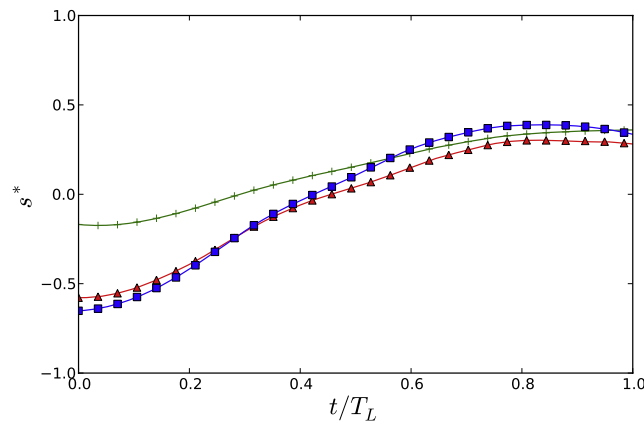


FIG. 11. Same as Fig. 10 but for the evolution of the shape factor s^* .

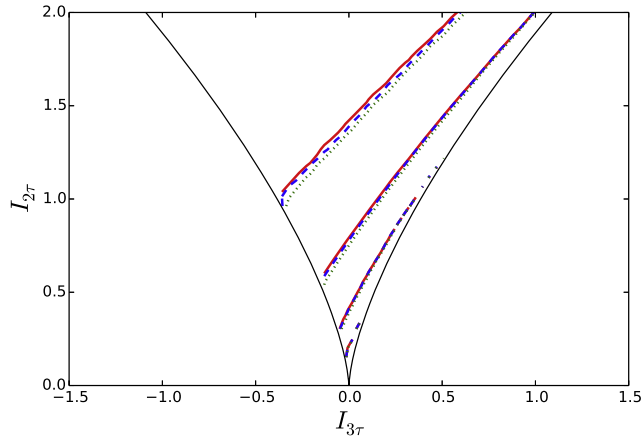


FIG. 12. The joint PDF of the invariants $I_{3\tau}$ and $I_{2\tau}$ of τ_{ij}^d with $\Delta = 16\delta x$. The values for the four groups of contours are, from bottom to top, 10, 1, 0.1, and 0.01, respectively. Red solid lines: $t/T_L \approx 0.7$, blue dashed lines: $t/T_L \approx 1.2$, and green dotted lines: $t/T_L \approx 2.1$.

calculation, we will use the nonlinear model T_{ij} to approximate the SGS stresses, i.e., we will look into the dynamical equations for invariants I_{2T} and I_{3T} instead of those for $I_{2\tau}$ and $I_{3\tau}$. As having been shown in Sec. III, the nonlinear model displays the same behavior as the true SGS stress regarding the preference of the rod-like structure. Also, it has been shown²² that τ_{ij} can be represented by a so-called multi-scale gradient expansion, in which each term represents the contribution from the motion in a given bandwidth. It is proven that the expansion is convergent, and the first truncation coincides with the nonlinear model T_{ij} given in Eq. (17). Besides, previous studies have shown that the geometrical structure of the nonlinear model is very similar to real SGS stress.^{19,28} Therefore, it is expected that the results obtained from the nonlinear model provide useful insight into the behaviours of the real SGS stress. The advantage of using the nonlinear model is that the algebra can be simplified and the interpretation of the results can be related to the fundamental nonlinear self-interaction term of the NS equations.

The equations for I_{2T} and I_{3T} may be derived from the equation for the filtered velocity gradient \tilde{A}_{ij} , which reads

$$D_t \tilde{A}_{ij} + \tilde{A}_{ik} \tilde{A}_{kj} = -\partial_{ij}^2 \tilde{p} + \partial_{jk}^2 (-\tau_{ik}) + \nu \nabla^2 \tilde{A}_{ij}, \quad (19)$$

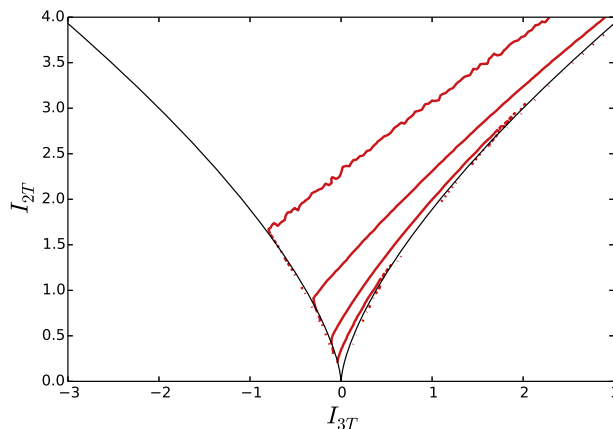


FIG. 13. The joint PDF of I_{3T} and I_{2T} . For filter scale $\Delta = 16\delta x$ at $t/T_L \approx 0.7$. The values of the contours are, from bottom to top, 1, 10^{-1} , 10^{-2} , and 10^{-3} .

where $D_t \equiv \partial_t + \tilde{u}_j \partial_j$ denotes the material derivative based on the filtered velocity field. Using Π_{ij} to denote the anisotropic part of the pressure Hessian and Y_{ij} to denote the anisotropic part of the subgrid-scale stress Hessian,

$$\Pi_{ij} = \partial_{ij}^2 \tilde{p} - \frac{1}{3} \delta_{ij} \nabla^2 \tilde{p}, \quad (20)$$

$$Y_{ij} = \partial_{jk}^2 (-\tau_{ik}) - \frac{1}{3} \delta_{ij} \partial_{mk}^2 (-\tau_{mk}). \quad (21)$$

The equations for I_{2T} and I_{3T} can be written as

$$\begin{aligned} D_t I_{3T} = & N_3 - C_{3ij} \Pi_{ij} + (C_{3ij} Y_{ij}^s + D_{3i} \varepsilon_{ikj} Y_{jk}) \\ & + \nu (C_{3ij} \nabla^2 \tilde{s}_{ij} + D_{3i} \nabla^2 \tilde{\omega}_i), \end{aligned} \quad (22)$$

$$\begin{aligned} D_t I_{2T} = & N_2 - C_{2ij} \Pi_{ij} + (C_{2ij} Y_{ij}^s + D_{2i} \varepsilon_{ikj} Y_{jk}) \\ & + \nu (C_{2ij} \nabla^2 \tilde{s}_{ij} + D_{2i} \nabla^2 \tilde{\omega}_i). \end{aligned} \quad (23)$$

The equations have been normalized by suitable powers of $\langle T_{ij} T_{ij} \rangle^{1/2}$ and the filter scale Δ . In the equations, N_2 and N_3 are the contributions due to the nonlinear self-interaction term in Eq. (19). Explicitly, we have

$$\begin{aligned} N_3 = & -3\tilde{\omega}^2 I_{2s} I_{3s} - \frac{2}{3} I_{2s}^2 I_{3s} + 2I_{3s} V^2 \\ & - \frac{13}{24} I_{3s} \tilde{\omega}^4 + \frac{1}{18} P I_{2s}^2 + \frac{17}{36} P \tilde{\omega}^2 I_{2s} \\ & - \frac{1}{6} P V^2 - \frac{1}{96} P \tilde{\omega}^4, \end{aligned} \quad (24)$$

$$N_2 = -2I_{2s} I_{3s} - \frac{7}{2} \tilde{\omega}^2 I_{3s} + \frac{5}{6} P I_{2s} + \frac{1}{8} P \tilde{\omega}^2. \quad (25)$$

In other words, N_3 and N_2 are given in terms of the invariants of the strain rate tensor \tilde{s}_{ij} and the vorticity $\tilde{\omega}_i$, including $\tilde{\omega}^2 \equiv \tilde{\omega}_i \tilde{\omega}_i$, $I_{2s} \equiv \tilde{s}_{ij} \tilde{s}_{ji} / 2$, $I_{3s} \equiv \tilde{s}_{ij} \tilde{s}_{jk} \tilde{s}_{ki} / 3$, $P \equiv \tilde{\omega}_i \tilde{s}_{ij} \tilde{\omega}_j$, and $V^2 \equiv V_i V_i$ with $V_i \equiv \tilde{s}_{ij} \tilde{\omega}_j$.

The second terms on the right hand sides of Eqs. (22) and (23) represent the effects of the anisotropic pressure Hessian Π_{ij} . The third terms are the contributions from the anisotropic SGS stress Hessian, where Y_{ij}^s represents the symmetric part of Y_{ij} . The last terms are the viscous contributions. C_{2ij} , C_{3ij} , D_{2i} , and D_{3i} are tensor functions of \tilde{s}_{ij} and $\tilde{\omega}_i$. Their expressions are given in Appendix B.

The dynamics of (I_{3T}, I_{2T}) is manifested in the evolution of the joint PDF $P(I_{3T}, I_{2T})$. The equation of $P(I_{3T}, I_{2T})$ is given by³

$$\begin{aligned} \frac{\partial P}{\partial t} = & -\frac{\partial}{\partial I_{3T}} \langle D_t I_{3T} | I_{2T}, I_{3T} \rangle P \\ & - \frac{\partial}{\partial I_{2T}} \langle D_t I_{2T} | I_{2T}, I_{3T} \rangle P. \end{aligned} \quad (26)$$

Using Eqs. (22) and (23), we see that the evolution of $P(I_{3T}, I_{2T})$ are controlled by four vector fields,

$$\mathbf{F}_n = (\langle N_3 | I_{3T}, I_{2T} \rangle, \langle N_2 | I_{3T}, I_{2T} \rangle), \quad (27)$$

$$\begin{aligned} \mathbf{F}_p = & -(\langle C_{3ij} \Pi_{ij} | I_{3T}, I_{2T} \rangle, \\ & \langle C_{2ij} \Pi_{ij} | I_{3T}, I_{2T} \rangle), \end{aligned} \quad (28)$$

$$\begin{aligned} \mathbf{F}_s = & (\langle C_{3ij} Y_{ij}^s + D_{3i} \varepsilon_{ikj} Y_{jk} | I_{3T}, I_{2T} \rangle, \\ & \langle C_{2ij} Y_{ij}^s + D_{2i} \varepsilon_{ikj} Y_{jk} | I_{3T}, I_{2T} \rangle), \end{aligned} \quad (29)$$

$$\begin{aligned} \mathbf{F}_v = & (\nu \langle C_{3ij} \nabla^2 \tilde{s}_{ij} + D_{3i} \nabla^2 \tilde{\omega}_i | I_{3T}, I_{2T} \rangle, \\ & \nu \langle C_{2ij} \nabla^2 \tilde{s}_{ij} + D_{2i} \nabla^2 \tilde{\omega}_i | I_{3T}, I_{2T} \rangle), \end{aligned} \quad (30)$$

which are defined in terms of the conditional averages at given I_{3T} and I_{2T} . We will call these vectors the probability flow vectors. The stream lines of these vector fields define the so-called

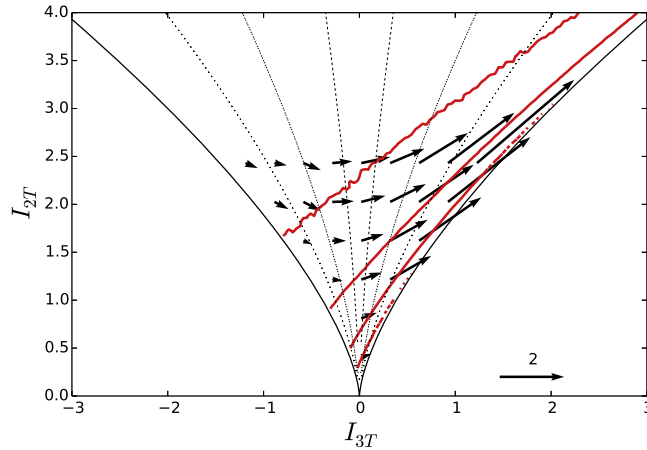


FIG. 14. The probability flow vector field \mathbf{F}_n for filter scale $\Delta = 16\delta x$. Red solid lines: the joint PDF of (I_{3T}, I_{2T}) . Dotted lines: linear relaxation.

conditional trajectories,²³ which show the most possible dynamical evolution of a given configuration (I_{3T}, I_{2T}) . In the following, we will present the results for these vector fields, calculated from the 256^3 DNS data (i.e., Case I above). The majority results are for filter scale $\Delta = 16\delta x$, where $\delta x \equiv \pi/128$ is the grid size.

The contribution from the nonlinear self-interaction term is shown in Fig. 14. The figure shows that the nonlinear term tends to push the phase point from the left half of the plane to the right and then away from the origin along the right boundary (the rod-like axisymmetric state). Its effects are much stronger for $I_{3T} > 0$ than for $I_{3T} < 0$. The overall effects are consistent with the known properties of the nonlinear term. For example, it has been observed that the nonlinear term has similar effects for the invariants of the strain rate tensor s_{ij} previously.^{23,24}

The probability flow vectors for the pressure Hessian contribution, \mathbf{F}_p , are plotted in Fig. 15. It is interesting to see that, overall, the pressure tends to oppose the nonlinear term. This trend is especially strong for $I_{3T} > 0$, where it acts to reduce the anisotropy of the SGS stress tensor, with the vectors pointing to the origin. When $I_{3T} < 0$, it tends to enhance the disk-like axisymmetric structure. These observations are consistent with previous results reported in, e.g., Ref. 18, where the effects of the pressure Hessian are studied in the phase space of the invariants of the velocity gradient tensor.

Recall that, for the Reynolds stress tensor, the tendency towards the rod-like axisymmetric state is a consequence of the pressure-strain-rate correlation. Therefore, we plot in Fig. 16 the

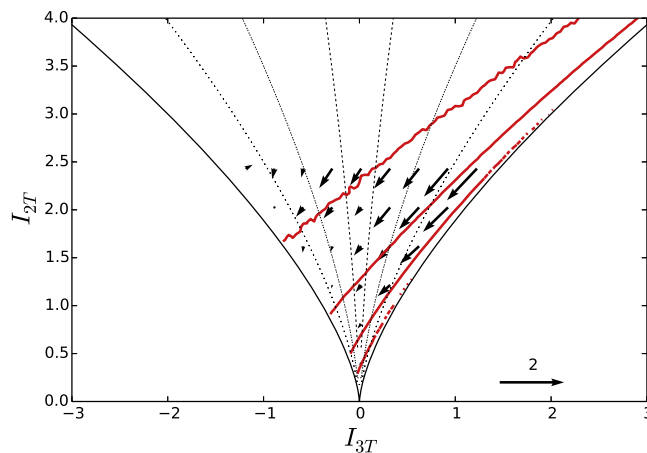


FIG. 15. Same as Fig. 14, but for the probability flow vector field \mathbf{F}_p .

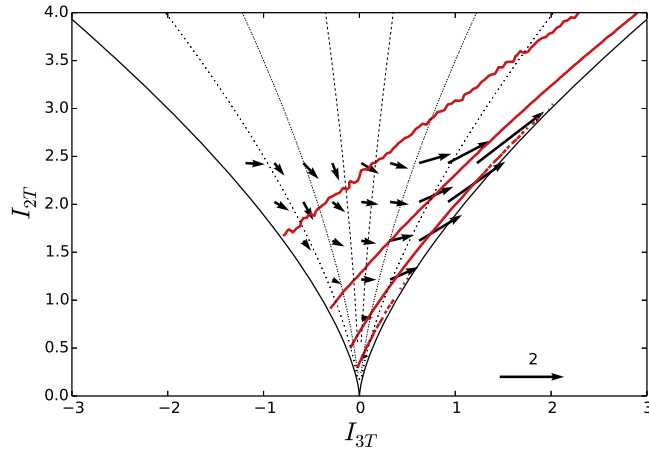


FIG. 16. Same as Fig. 14, but for the probability flow vector field $\mathbf{F}_n + \mathbf{F}_p$.

contributions from the sum of the nonlinear term and the pressure term. Apart from some statistical scattering on the top-left part, the combined vector field points to the positive I_{3T} direction in most region of the Lumley triangle. It becomes stronger near the right boundary, where it tends to point away from the origin. Therefore, in combination, the two terms would move the phase point towards the rod-like axisymmetric state. The result is consistent with the results shown previously, as in Figs. 7, 9, and 10, where the trajectories are found to be attracted to the right boundary before they return towards the origin. However, Figs. 14, and 15 show that the driver of the process is the nonlinear self-interaction term, whereas the pressure mainly acts to counter its effects.

The SGS and viscous contributions are given in Figs. 17 and 18. The SGS contribution moves the phase point from the positive half plane where $I_{3T} > 0$ to the negative half plane. In particular, it enhances the probability for the disk-like structure and promotes stronger anisotropy by pushing the stress tensor away from the origin along the left boundary of the triangle. The latter effect differentiates it from the pressure Hessian term. The viscous diffusion term has similar effects as the SGS stress; however, its magnitude is much smaller. Overall, the effects of these two contributions are to balance the effects of the nonlinear self-interaction term.

The same behaviors are observed at different filter scales. As an illustration, we show the result for the sum of the nonlinear term and the pressure term in Fig. 19, for $\Delta = 32\delta x$, which clearly displays same trends as shown in Fig. 16. For other contributions, the same behaviours are also observed at this filter scale, as well as $\Delta = 64\delta x$.

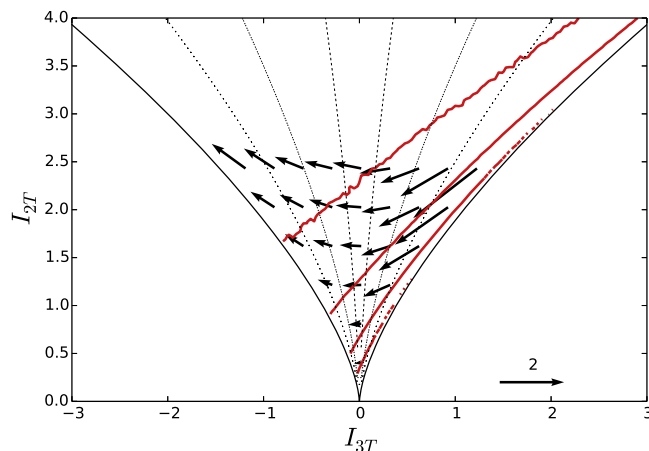
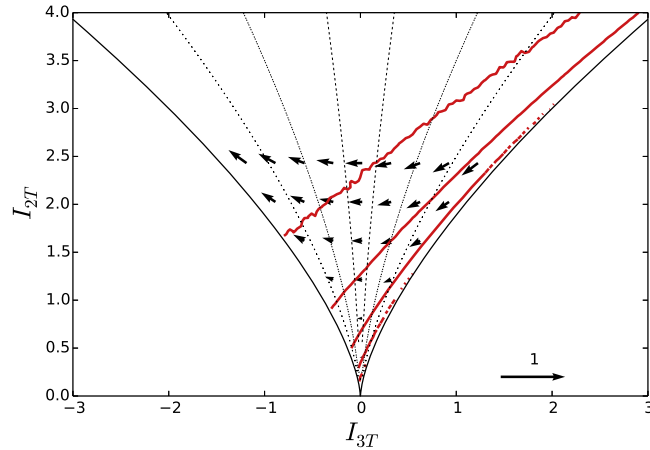
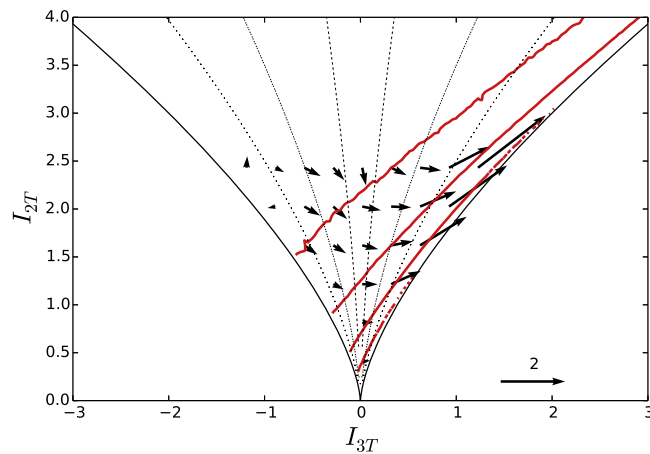


FIG. 17. The probability flow vector field \mathbf{F}_s for filter scale $\Delta = 16\delta x$.

FIG. 18. The probability flow vector field \mathbf{F}_v for filter scale $\Delta = 16\delta x$.FIG. 19. The probability flow vector field $\mathbf{F}_n + \mathbf{F}_p$ for filter scale $\Delta = 32\delta x$.

V. CONCLUSIONS

In this paper, we have looked into the tendency for turbulent stresses to evolve towards the rod-like axisymmetric configuration, where the tensors have two negative, equal eigenvalues, and a positive one. Such a tendency has been conclusively observed for the subgrid-scale stress tensor. The same has also been suggested for the Reynolds stress tensor. However, because the available data are limited, it has not been generally accepted. The first contribution of the paper is to confirm that the observation for the Reynolds stress tensor is universal. The finding is made possible by a new method to generate synthetic anisotropic turbulent fields, the so-called constrained multi-turnover Lagrangian map we have developed recently. Using the method, we generate realistic initial turbulent velocity fields with any prescribed anisotropic Reynolds stress tensor not achievable before, hence verifying the universality of the tendency with direct numerical simulations.

We then look into the dynamical mechanisms of the tendency using direct numerical simulations data. It is shown that the trend is essentially due to the nonlinear self-interaction process of the Navier-Stokes equations, which tends to produce the rod-like axisymmetric state with ever stronger anisotropy. The non-local pressure Hessian tends to reduce the anisotropy of the tensor when it is already in the rod-like structure. Otherwise, it generally tends to push the tensor towards disk-like axisymmetric state. These observations highlight the different roles of the pressure and

the nonlinear interaction term thus provide additional insights into the common observation that the return-to-isotropy process is due to the pressure-strain-rate correlation.

The SGS contribution also tends to counter the effects of the nonlinear term, but in a different way. In particular, the SGS contribution favors disk-like structures, i.e., those with two large eigenvalues. It also tends to increase the degree of anisotropy for the disk-like axisymmetric structures. The viscous contribution shows similar trends as the SGS contribution, but with much smaller magnitudes.

To conclude, we note that the constrained multi-turnover Lagrangian map is an essential tool for this study. One can envision many other applications for the method. Our investigation into the evolution of the turbulent stresses provides new insights on the dynamics towards the rod-like axisymmetric state. It is our hope that the results will be useful for refining current models for the turbulent stresses.

APPENDIX A: THE OPTIMALITY SYSTEM OF THE CONSTRAINED MULTI-TURNOVER LAGRANGIAN MAP

1. The continuous versions of the adjoint operators

The MTLM takes a random velocity field $\boldsymbol{\varphi}(\mathbf{x})$ as the input and generates an isotropic synthetic velocity field with a prescribed energy spectrum $E_p(k)$. As a first step of the mapping, the divergence of $\boldsymbol{\varphi}(\mathbf{x})$ is removed by projection, giving $\mathbf{u}_{10}(\mathbf{x}) \equiv \mathcal{P}\boldsymbol{\varphi}(\mathbf{x})$, where \mathcal{P} is the usual projection operator. Letting $\hat{\mathbf{v}}(\mathbf{k})$ be the Fourier transform of a velocity field $\mathbf{v}(\mathbf{x})$, \mathcal{P} is defined as

$$\mathcal{P}\hat{\mathbf{v}}(\mathbf{k}) = [1 - k^{-2}\mathbf{k} \otimes \mathbf{k}]\hat{\mathbf{v}}(\mathbf{k}), \quad (\text{A1})$$

with $k = |\mathbf{k}|$ and \mathbf{k} being the wavenumber. A sequence of operations are then applied to \mathbf{u}_{10} . The operations are defined at a hierarchy of M length scales $\ell_n = 2^{-n}L$ ($n = 1, 2, \dots, M$), where L is the integral length scale. Each scale ℓ_n corresponds to one iteration of the operations. At each iteration, the velocity field generated from the previous iteration is used as the input. As a consequence, we generate $M + 1$ velocity fields from $\boldsymbol{\varphi}$ after M iterations: $\mathbf{u}_{10}, \mathbf{u}_{20}, \dots, \mathbf{u}_{M0}$, and \mathbf{u} , where \mathbf{u} is the final MTLM synthetic field. Velocity field \mathbf{u}_{n0} is the output of the $(n - 1)$ th iteration and the input for the n th iteration.

At the n th iteration, we start with \mathbf{u}_{n0} and the following operators are applied: the advection operator, the projection operator, and the rescaling operator. The procedure is as follows:

1. \mathbf{u}_{n0} is low-pass filtered to produce $\mathbf{u}_{n1} \equiv \mathcal{G}_n\mathbf{u}_{n0}$, where \mathcal{G}_n represents the filtering operation with length scale ℓ_n . The high wavenumber components of \mathbf{u}_{n0} are kept unchanged.
2. Advection operator \mathcal{A}_n and the projection operator \mathcal{P} are then applied to \mathbf{u}_{n1} m_n times, giving velocity field \mathbf{u}_{n2} , i.e., $\mathbf{u}_{n2} \equiv (\mathcal{P}\mathcal{A})^{m_n}\mathbf{u}_{n1}$. \mathcal{A}_n is the advection operator with advection time t_n , defined as follows for a generic velocity field $\mathbf{v}(\mathbf{x})$:

$$\mathcal{A}_n\mathbf{v}(\mathbf{x}) = \int W(\mathbf{x} - \mathbf{y} - \mathbf{v}(\mathbf{y})t_n)\mathbf{v}(\mathbf{y})d\mathbf{y}, \quad (\text{A2})$$

where W is a weighting function.¹⁶ The advection time t_n and m_n are specified below. \mathcal{A}_n is called the advection operator because $\mathcal{A}_n\mathbf{v}(\mathbf{x})$ represents the solution of the Riemann equation $\partial_t\mathbf{v} + \mathbf{v} \cdot \nabla\mathbf{v} = 0$ when the weight W is taken as the Dirac-delta function.

3. \mathbf{u}_{n2} is rescaled, giving $\mathbf{u}_{n3} = \mathcal{R}_n\mathbf{u}_{n2}$, where \mathcal{R}_n is the rescaling operator associated with \mathbf{u}_{n2} , defined by

$$\mathcal{R}_n\hat{\mathbf{u}}_{n2}(\mathbf{k}) = \left[\frac{E_p(k)}{E_n(k)} \right]^{1/2} \hat{\mathbf{u}}_{n2}(\mathbf{k}), \quad (\text{A3})$$

where $\hat{\mathbf{u}}_{n2}(\mathbf{k})$ is the Fourier transform of \mathbf{u}_{n2} and $E_n(k)$ its energy spectrum.

4. \mathbf{u}_{n3} is merged with the high wavenumber components of \mathbf{u}_{n0} to generate the final field of current iteration, $\mathbf{u}_{(n+1)0}$, leading to

$$\mathbf{u}_{(n+1)0} = \mathbf{u}_{n3} + \mathcal{G}_n^c\mathbf{u}_{n0},$$

where $\mathcal{G}_n^c = 1 - \mathcal{G}_n$.

Combining the operations together, we obtain the final MTLM velocity field $\mathbf{u} = \mathcal{M}\boldsymbol{\varphi}$ (i.e., Eq. (8)), with

$$\mathcal{M} = \prod_{n=1}^M [\mathcal{R}_n(\mathcal{P}\mathcal{A}_n)^{m_n} \mathcal{G}_n + \mathcal{G}_n^c] \mathcal{P}. \quad (\text{A4})$$

The product is ordered such that from left to right n decreases from M to 1. The advection time scale t_n in operator \mathcal{A}_n is given by

$$t_n = \frac{\ell_n}{u'_n},$$

where

$$u'_n = \left(\frac{2}{3} \int_0^{k_{c,n}} E_p(k) dk \right)^{1/2},$$

with $k_{c,n} = \pi/\ell_n$ being the cutoff wavenumber corresponding to ℓ_n . On the other hand, the parameter m_n is given by

$$m_n = \frac{\ell_n^{2/3} \epsilon^{-1/3}}{t_n}, \quad (\text{A5})$$

where ϵ is the energy dissipation rate corresponding to the prescribed energy spectrum. For more details, see Refs. 15 and 17. In the numerical implementation of the MTLM map, the operations are applied recursively over a set of finer and finer grids defined by the length scales. In order to evaluate the weight function in the advection map \mathcal{A}_n , we need to track the movement of Lagrangian fluid particles, hence the name ‘‘Lagrangian map.’’

In the CMTLM method, we solve an optimization problem to find the $\boldsymbol{\varphi}$ that minimizes the difference between \mathbf{u} and some target function. For present study, we solve the state equation given by Eq. (8) and the adjoint equation given by Eq. (13). We also need the gradient of the cost function to perform steepest descent iterations. The gradient is given by¹⁵

$$\frac{\mathcal{D}J}{\mathcal{D}\boldsymbol{\varphi}} = \frac{\delta \mathcal{L}}{\delta \boldsymbol{\varphi}} \Big|_{\mathbf{u}, \boldsymbol{\xi}} = -\mathcal{M}^+ \boldsymbol{\xi}, \quad (\text{A6})$$

where

$$\mathcal{M}^+ = \mathcal{P} \prod_{n=1}^M (\mathcal{B}_n + \mathcal{G}_n^c) = \mathcal{P} \sum_{i=1}^M \mathcal{G}_{i-1}^c \prod_{n=i}^M \mathcal{B}_n \quad (\text{A7})$$

and

$$\mathcal{B}_n = \mathcal{G}_n \mathcal{D}_n^{A+} \mathcal{D}_n^{R+}. \quad (\text{A8})$$

\mathcal{D}_n^{A+} is the adjoint of the tangent operator of the composite operator $(\mathcal{P}\mathcal{A}_n)^{m_n}$ applied to \mathbf{u}_{n1} and \mathcal{D}_n^{R+} is the adjoint of the tangent operator of the rescaling operator \mathcal{R}_n applied to \mathbf{u}_{n2} . Note that, for simplicity, we sometimes speak of the adjoint of a nonlinear operator, even though in this case, it is actually the adjoint of the tangent operator of the nonlinear operator.

For completeness, we give below the expressions of the above adjoint operators for generic velocity fields. We use \mathcal{R}_v to denote the rescaling operator applied to a generic velocity field \mathbf{v} , i.e.,

$$\mathcal{R}_v \hat{\mathbf{v}}(\mathbf{k}) = \left[\frac{E_p(k)}{E_v(k)} \right]^{1/2} \hat{\mathbf{v}}(\mathbf{k}), \quad (\text{A9})$$

where $E_v(k)$ is the energy spectrum of $\mathbf{v}(\mathbf{x})$. Using \mathcal{D}_v^{R+} to denote the adjoint of \mathcal{R}_v , the operation of \mathcal{D}_v^{R+} on a test function $\boldsymbol{\eta}(\mathbf{x})$ is given by¹⁵

$$\mathcal{D}_v^{R+} \hat{\boldsymbol{\eta}}(\mathbf{k}) = \mathcal{R}_v \hat{\boldsymbol{\eta}}(\mathbf{k}) - \frac{E_p(k)^{1/2}}{E_v(k)^{3/2}} \zeta_{v\eta}(k) \hat{\mathbf{v}}(\mathbf{k}), \quad (\text{A10})$$

where $\hat{\eta}$ is the Fourier transform of η and $\zeta_{v\eta}(k)$ is the co-spectrum between \mathbf{v} and η , defined as

$$\zeta_{v\eta}(k) = \frac{1}{2} \oint_{S_k} \hat{\eta}^* \cdot \hat{\mathbf{v}} dS. \tag{A11}$$

The integration is taken over the surface $S_k = \{\mathbf{k} : |\mathbf{k}| = k\}$ in the Fourier space and the asterisk denotes complex conjugate. Given \mathcal{D}_v^{R+} , \mathcal{D}_n^{R+} is found by simply replacing \mathbf{v} with \mathbf{u}_n .

As for \mathcal{D}_n^{A+} , we may write

$$\mathcal{D}_n^{A+} = \mathcal{D}_{n0}^{A+} \mathcal{D}_{n1}^{A+} \dots \mathcal{D}_{n(m_n-1)}^{A+}, \tag{A12}$$

where \mathcal{D}_{ni}^{A+} is the adjoint of $\mathcal{P}\mathcal{A}_n$ when the latter is applied to velocity field $(\mathcal{P}\mathcal{A}_n)^i \mathbf{u}_{n1}$. To find the expression for \mathcal{D}_{ni}^{A+} , we need only to consider \mathcal{D}_v^{A+} , namely the adjoint of $\mathcal{P}\mathcal{A}$ when it is applied to a generic velocity field \mathbf{v} . The expression for \mathcal{D}_v^{A+} acting on a test function $\eta(\mathbf{x})$ is given in Ref. 15 as follows:

$$\begin{aligned} \mathcal{D}_v^{A+} \eta(\mathbf{x}) &= \int d\mathbf{y} W(\mathbf{h}) \mathcal{P}\eta(\mathbf{y}) \\ &+ \int d\mathbf{y} W(\mathbf{h}) [\nabla_y \mathcal{P}\eta(\mathbf{y})] \cdot \mathbf{v}(\mathbf{x}) t, \end{aligned} \tag{A13}$$

in which $\mathbf{h} \equiv \mathbf{y} - \mathbf{x} - \mathbf{v}(\mathbf{x})t$ and t is the advection time parameter for the advection operator \mathcal{A} . ∇_y denotes the gradient operator with \mathbf{y} as the variables.

2. The adjoint of the discretized advection operator

Equation (A13) gives the continuous version of \mathcal{D}_v^{A+} , which is the adjoint of the continuous version of the composite operator $\mathcal{P}\mathcal{A}$ applied to velocity field \mathbf{v} . In the numerical implementation, one will have to discretize \mathcal{D}_v^{A+} . This method is an example of the so-called ‘‘differentiate-then-discretize’’ method,²⁵ which is used in Ref. 15. Another possible way is to use the ‘‘discretize-then-differentiate’’ method, where one starts with the discretized version of $\mathcal{P}\mathcal{A}$ and then derives the adjoint of the discretized operator.²⁵ It turns out that treating the advection operator \mathcal{A} with the latter method provides better convergence in the present study. We thus derive below the adjoint of the discretized advection operator, which has not been obtained before.

Note that in the continuous version, we have combined \mathcal{P} with \mathcal{A} . However, it is not convenient to do so in the discretized version, because \mathcal{P} and \mathcal{A} will have to be implemented, respectively, in the Fourier and the physical spaces. Therefore, for the discretized version, we will derive the adjoint for \mathcal{A} only, which we will call \mathcal{T}_v^{A+} . It is easy to show that the adjoint of the discretized $\mathcal{P}\mathcal{A}$ is the product $\mathcal{T}_v^{A+}\mathcal{P}$. Therefore, we can easily obtain the discretized equivalence to \mathcal{D}_v^{A+} .

We assume \mathcal{A} is applied to velocity field $\mathbf{v}(\mathbf{x})$ and we let $\mathbf{v}_a = \mathcal{A}\mathbf{v}$. The velocity fields are discretized on a set of grid points $\mathbf{x}^{(i)}$, $i = 1, 2, \dots, N$, with N being the number of grid points. Let $\mathbf{v}_a^{(i)}$ and $\mathbf{v}^{(i)}$ be the velocities on grid point $\mathbf{x}^{(i)}$. We will only consider the weight function that is implemented numerically in our studies,

$$W(\mathbf{x}) = \frac{H(|\mathbf{x}|^{-1} - d_c^{-1})}{|\mathbf{x}|}, \tag{A14}$$

where d_c is a cutoff length and $H(\cdot)$ is the Heaviside function. We introduce notations

$$\mathbf{h}^{(ij)} = \mathbf{x}^{(i)} - \mathbf{x}^{(j)} - \mathbf{v}^{(j)}t \tag{A15}$$

and

$$w_{ij} = W(\mathbf{h}^{(ij)}) = \frac{H(|\mathbf{h}^{(ij)}|^{-1} - d_c^{-1})}{|\mathbf{h}^{(ij)}|}. \tag{A16}$$

Letting $s_i = (\sum_{j=1}^N w_{ij})^{-1}$, where the summation is taken over all the grid points, we have the following relation:

$$\mathbf{v}_a^{(i)} = s_i \sum_{j=1}^N w_{ij} \mathbf{v}^{(j)}, \tag{A17}$$

which defines the discretized version of the advection operator \mathcal{A} . If we order $\mathbf{v}^{(j)}$ into a column vector with x components first and then y and z components, then the operator is a 3×3 diagonal block matrix with three identical $N \times N$ matrices on the diagonal. The (i, j) entry of this $N \times N$ matrix is $s_i w_{ij}$.

The tangent operator of \mathcal{A} is defined by the differential of $\mathbf{v}_a^{(i)}$. Using Eq. (A17), we obtain

$$\begin{aligned} \delta \mathbf{v}_a^{(i)} &= s_i \sum_{j=1}^N \left[t(\mathbf{v}^{(j)} - \mathbf{v}_a^{(i)}) w_{ij}^3 \mathbf{h}^{(ij)} \cdot \delta \mathbf{v}^{(j)} \right] \\ &+ s_i \sum_{j=1}^N w_{ij} \delta \mathbf{v}^{(j)}. \end{aligned} \tag{A18}$$

The tangent operator is the coefficient matrix for $\delta \mathbf{v}^{(j)}$. The adjoint operator \mathcal{T}_v^{A+} is simply the transpose of the tangent operator. To write down the expression for \mathcal{T}_v^{A+} , we consider a test function $\boldsymbol{\eta}(\mathbf{x})$. Let $\boldsymbol{\eta}_a = \mathcal{T}_v^{A+} \boldsymbol{\eta}$, and $\boldsymbol{\eta}^{(i)}$ and $\boldsymbol{\eta}_a^{(i)}$ be the values of the two functions at $\mathbf{x}^{(i)}$, respectively. Then, from Eq. (A18), we find that

$$\begin{aligned} \boldsymbol{\eta}_a^{(j)} &= t \sum_{i=1}^N s_i w_{ij}^3 \mathbf{h}^{(ij)} (\mathbf{v}^{(j)} - \mathbf{v}_a^{(i)}) \cdot \boldsymbol{\eta}^{(i)} \\ &+ \sum_{i=1}^N s_i w_{ij} \boldsymbol{\eta}^{(i)}, \end{aligned} \tag{A19}$$

which defines the adjoint of the discretized advection operator. For given $\boldsymbol{\eta}^{(i)}$, $\boldsymbol{\eta}_a^{(j)}$ is evaluated similarly to the discretized advection operator, i.e., via Lagrangian particle tracking (cf. Ref. 17).

In this paper, Eq. (A19) is used whenever the adjoint of the advection operator needs to be evaluated. This method is different from the one in our previous study reported in Ref. 15, where the continuous version given in Eq. (A13) is used.

APPENDIX B: EXPRESSIONS FOR THE COEFFICIENTS IN THE EQUATIONS FOR I_{2T} AND I_{3T}

The expressions for the coefficients are given as follows:

$$C_{2ij} = f_1 \tilde{s}_{ij} - 2V_i \tilde{\omega}_j, \tag{B1}$$

$$D_{2i} = f_2 \tilde{\omega}_i - 2\tilde{s}_{ij} V_j, \tag{B2}$$

$$C_{3ij} = f_3 \tilde{s}_{ij} + 4f_4 \tilde{s}_{ij}^2 + f_4 \tilde{\omega}_i \tilde{\omega}_j + f_5 V_i \tilde{\omega}_j, \tag{B3}$$

$$D_{3i} = f_6 \tilde{\omega}_i + 2f_4 V_i + f_5 \tilde{s}_{ij} V_j, \tag{B4}$$

where $V_i = \tilde{s}_{ij} \tilde{\omega}_j$ and

$$f_1 = \frac{7}{6} \tilde{\omega}^2 + \frac{2}{3} I_{2s}, \quad f_2 = \frac{\tilde{\omega}^2}{12} + \frac{7}{3} I_{2s}, \tag{B5}$$

$$f_3 = \frac{11}{72} \tilde{\omega}^4 - \frac{2}{9} I_{2s}^2 + \frac{11}{9} I_{2s} \tilde{\omega}^2 - \frac{2}{3} V^2, \tag{B6}$$

$$f_4 = \frac{I_{3s}}{2} + \frac{P}{8}, \quad f_5 = -\frac{4}{3} I_{2s} - \frac{\tilde{\omega}^2}{3}, \tag{B7}$$

$$f_6 = \frac{11}{9} I_{2s}^2 + \frac{11}{18} I_{2s} \tilde{\omega}^2 - \frac{V^2}{3} - \frac{\tilde{\omega}^4}{144}. \tag{B8}$$

- ¹ P. Sagaut, *Large Eddy Simulation for Incompressible Flows: An Introduction*, 2nd ed. (Springer, 2002).
- ² C. Meneveau and J. Katz, "Scale-invariance and turbulence models for large-eddy simulation," *Annu. Rev. Fluid Mech.* **32**, 1–32 (2000).
- ³ S. B. Pope, *Turbulent Flows* (Cambridge University Press, Cambridge, 2000).
- ⁴ J. Lumley, "Computational modelling of turbulent flows," *Adv. Appl. Mech.* **18**, 123 (1978).
- ⁵ P.-A. Krogstad and L. Torbergsen, "Invariant analysis of turbulent pipe flow," *Flow, Turbul. Combust.* **64**, 161 (2000).
- ⁶ A. J. Simonsen and P.-A. Krogstad, "Turbulent stress invariant analysis: Clarification of existing terminology," *Phys. Fluids* **17**, 088103 (2005).
- ⁷ M. K. Chung and S. K. Kim, "A nonlinear return-to-isotropy model with Reynolds number and anisotropy dependency," *Phys. Fluids* **7**, 1425 (1995).
- ⁸ K.-S. Choi and J. L. Lumley, "The return-to-isotropy of homogeneous turbulence," *J. Fluid Mech.* **436**, 59 (2001).
- ⁹ D. C. Haworth and S. B. Pope, "A generalized Langevin model for turbulent flows," *Phys. Fluids* **29**, 387 (1986).
- ¹⁰ S. Sarkar and C. G. Speziale, "A simple nonlinear model for the return to isotropy in turbulence," *Phys. Fluids A: Fluid Dyn. (1989-1993)* **2**, 84–93 (1990).
- ¹¹ C. G. Speziale, S. Sarkar, and T. B. Gatski, "Modelling the pressure-strain correlation of turbulence: An invariant dynamical systems approach," *J. Fluid Mech.* **227**, 245 (1991).
- ¹² T.-H. Shih and J. L. Lumley, "Critical comparison of second-order closure with direct numerical simulations of homogeneous turbulence," *AIAA J.* **31**, 663 (1993).
- ¹³ M. J. Lee, "Numerical experiments on the structure of homogeneous turbulence," Ph.D. thesis, Stanford University, CA, USA, 1985.
- ¹⁴ M. J. Lee and W. C. Reynolds, "On the structure of homogeneous turbulence," *Turbul. Shear Flows* **5**, 54–66 (1987).
- ¹⁵ Y. Li and C. Rosales, "Constrained multi-scale turnover Lagrangian map for anisotropic synthetic turbulence: *A priori* tests," *Phys. Fluids* **26**, 075102 (2014).
- ¹⁶ C. Rosales and C. Meneveau, "A minimal multiscale Lagrangian map approach to synthesize non-Gaussian turbulent vector fields," *Phys. Fluids* **18**, 075104 (2006).
- ¹⁷ C. Rosales and C. Meneveau, "Anomalous scaling and intermittency in three-dimensional synthetic turbulence," *Phys. Rev. E* **78**, 016313 (2008).
- ¹⁸ L. Chevillard, E. Leveque, F. Taddia, C. Meneveau, H. Yu, and C. Rosales, "Local and nonlocal pressure Hessian effects in real and synthetic fluid turbulence," *Phys. Fluids* **23**, 095108 (2011).
- ¹⁹ B. Tao, J. Katz, and C. Meneveau, "Statistical geometry of subgrid-scale stresses determined from holographic particle image velocimetry measurements," *J. Fluid Mech.* **457**, 35–78 (2002).
- ²⁰ A. Leonard, "Energy cascade in large-eddy simulations of turbulent fluid flows," *Adv. Geophys.* **18**, 237 (1974).
- ²¹ R. A. Clark, J. H. Ferziger, and W. C. Reynolds, "Evaluation of subgrid-scale models using an accurately simulated turbulent flow," *J. Fluid Mech.* **91**, 1–16 (1979).
- ²² G. L. Eyink, "Multi-scale gradient expansion of the turbulent stress tensor," *J. Fluid Mech.* **549**, 159–190 (2006).
- ²³ A. Ooi, J. Martin, J. Soria, and M. S. Chong, "A study of evolution and characteristics of the invariants of the velocity-gradient tensor in isotropic turbulence," *J. Fluid Mech.* **381**, 141–174 (1999).
- ²⁴ K. K. Nomura and G. K. Post, "The structure and dynamics of vorticity and rate of strain in incompressible homogeneous turbulence," *J. Fluid Mech.* **377**, 65–97 (1998).
- ²⁵ M. D. Gunzburger, *Perspectives in Flow Control and Optimization* (SIAM, 2003).
- ²⁶ J. Nocedal and S. J. Wright, *Numerical Optimization* (Springer, 1999).
- ²⁷ T. S. Lund and M. M. Rogers, "An improved measure of strain state probability in turbulent flows," *Phys. Fluids* **6**, 1838–1847 (1994).
- ²⁸ K. Horiuti, "Roles of non-aligned eigenvectors of strain-rate and subgrid-scale stress tensors in turbulence generation," *J. Fluid Mech.* **491**, 65–100 (2003).